The Korean Journal of Rheology,
Vol. 11, No. 1, March 1999 pp. 18-27

<연구논문>

열성형공정의 3차원 유한요소해석

남기준 · 손동수 · 이재욱
서강대학교 공과대학 화학공학과
(1999년 1월 22일)

3-Dimensional Finite Element Analysis of Thermoforming Processes

G.J. Nam, D.S. Son and J.W. Lee
Department of Chemical Engineering, Sogang University, Seoul 121-742, Korea
(Received January 22, 1999)

요 약

본 연구에서는 3차원 열성형 공정 알고리듬과 이에 membrane approximation을 도입한 근사적인 알고리듬을 개발하였고, 이 알고리듬을 이용하여 몇몇 열성형계에 대한 수치모사를 수행하여 그 결과를 비교 분석하였다. 3차원 알고리듬의 경우에는 구성한 유한요소 평형 방정식에 벌칙함수를 도입하여 비압축성 조건을 만족시켜 해를 얻었으며, membrane approximation을 도입한 알고리듬의 경우에는 두께 방향의 응력을 무시하여 구성한 방정식으로부터 해를 얻었다. 구성방정식은 2nd Piola-Kirchhoff 응력 텐서와 Cauchy-Green 변형 텐서를 사용하여 표현하였고 수지의 물질 모델식으로는 2항의 Mooney-Rivlin 모델을 사용하였으며, total Lagrangian coordinate를 도입하여 지배방정식을 유한요소화함으로써 알고리듬을 구성하였다. 대상계로 선정한 사각평판 수지의 자유 부풀림 거동과 금형이 있는 경우에서의 수지의 부풀림 거동을 3차원 알고리듬과 membrane approximation 알고리듬을 각각 이용하여 분석하였으며 3차원 알고리듬의 경우 clamping 부분의 경계조건을 달리하여 결과를 비교하였다. 금형이 있는 계에 대해서는 slip 경계조건과 no-slip 경계조건을 각각 부여하여 수치모사를 수행, 수지의 변형거동과 응력분포를 비교 분석하였으며, 두께를 달리한 수지에 대해 두께 방향의 응력을 비교 분석함으로써 membrane approximation 알고리듬의 한계에 대하여 논하였다. 한편 수지 온도 변화에 따른 성형품의 두께 분포의 변화를 살펴보기 위하여 ABS 수지를 대상으로 하여 137.8°C에서 171.1°C 사이의 온도에서 수행한 인장 실험 데이터를 수치모사에 사용하였다. 그 결과 수지의 온도가 높을수록 두께의 표준편차가 감소하여 균일한 두께 분포를 얻을 수 있음을 확인하였고 이는 수지의 흐름성이 증가함으로써 나타나는 현상으로 해석할 수 있다.

Abstract—Predicting the deformation behaviors of sheets in thermoforming processes has been a daunting challenge due to the strong nonlinearities arising from very large deformations, mold-polymer contact condition and hyperelasticity constitutive equations. Nonlinear numerical analysis is always required to face this challenge especially for realistic processing conditions. In this study a 3-D algorithm and the membrane approximation are developed for thermoforming processes. The constitutive equation is expressed in terms of the 2nd Piola-Kirchhoff stress tensor and the Cauchy-Green deformation tensor. The 2-term Mooney-Rivlin model is used for the material model equation. The algorithm is established by the finite element formulation employing the total Lagrangian coordinate. The deformation behavior and the stress distribution results of 3-D algorithm with various point boundary conditions are compared to those of the membrane approximation algorithm. Also, the slip boundary condition and the no-slip boundary condition are applied for the systems that have molds. Finally, the effect of sheet temperatures on the final thickness distribution is investigated for the ABS material.

Keywords: Thermoforming Process, Finite Element Method, 3-D Analysis, Membrane Approximation, Total Lagrangian Formulation

1. Introduction

Thermoforming process has become one of the fastest growing plastics manufacturing methods since the commercialization of thermoplastic materials is relatively easy due to its superior adaptability, low initial investment, and excellent repeating qualities. In addition, it offers fast and uniform forming, lending itself to automation and long-term production runs. With its relatively fast molding cycles and comparatively inexpensive mold costs, thermoforming process is often chosen as the most cost-effective manufacturing method over all the other processes.

In the thermoforming process, thermoplastic sheets are heated above the glass transition temperature ahead of being formed, and then vacuum is applied until the desired shape of sheets is obtained. To shape a flat sheet

into a desired form and compel it to follow the contours of the adjacent mold, external forces must be applied. The energy level of this force should be adjustable so that the plastic sheet can either be eased into the coerced shape or, if necessary, explosively thrust into its new shape.

The thermoforming process, however, has difficulty in finding the optimal process conditions of certain systems under the process since the material experiences large deformation, and its behaviors are nonlinear. In the 1960s, to manufacture a new product a lot of ordeals such as finding the appropriate shape of the mold, temperature, and pressure of the process, arose, and exhaustive trial-and-errors were inevitable. This caused unnecessary waste of time and expenses. Therefore, the simulation algorithm which can predict the deforming behaviors of the material in the process will eliminate or significantly reduce the conventional trial-and-error runs. By the late 1970s, responding to the demand, the study on the development of the simulation algorithm began.

Several investigators have modeled the thermoforming process using rubber elasticity material models. It was J. T. Oden who applied the finite element method to the thermoforming process simulation for the first time[1]. They solved the problem of the inflation of a circular membrane with hyperelastic material properties subject to an increasing uniform pressure. Later, W. W. Feng extended the work of Oden. In his work he used the concept of the minimization of the total potential energy and performed the analysis of the thickness distribution[2]. By the late 1980s the equilibrium equation between the internal energy of the material to be deformed and the external force applied to the material began to be used in the solution algorithm. deLorenzi, et al. studied the 2-dimensional inflation algorithm using the Green-Lagrange deformation tensor and the 2nd Piola-Kirchhoff stress tensor[3]. Mooney-Rivlin and Ogden rubber elastic material models were implemented.

Recently, studies on the 3-dimensional simulation including viscoelastic material models such as K-BKZ model are being conducted in many research institutes[4-5, 16-19]. All these works were performed with membrane approximation, however.

2. Theory

2.1 Finite Element Formulation

For typical finite element formulations, it is assumed that the relationship between stresses and strains is linear when the displacements are sufficiently small. The total potential energy Π, with this assumption, in a static analysis of solids and structures including the thermoforming process is[6]

$$\prod = \frac{1}{2} \int_v \tau_{ij} e_{ij} \, dV - \int_s f_i^s u_i^s \, dS \tag{1}$$

The governing equation is obtained from the condition of minimizing the total potential energy Π, which leads to

$$\delta\prod = \int_v \tau_{ij} \delta e_{ij} \, dV - \int_s f_i^s \delta u_i^s \, dS = 0 \tag{2}$$

where the first term in eq. (2) represents the internal force that corresponds to the stress in the material, and the second term the externally applied force. Eqs. (1) and (2) lie under the assumption of small deformation. However, in the case of large deformation, the equilibrium of the body considered must be established in the current configuration, and then the problem turns nonlinear and this is the case in real systems. It is necessary to employ an incremental formulation and to use a time variable to describe the loading and the motion of the body. This concept leads to eq. (3), which expresses the total potential energy Π of a nonlinear analysis, which is similar to eq. (1) for a linear analysis.

$$\begin{aligned} \prod &= \frac{1}{2} \int_{t+\Delta t_V} {}^{t+\Delta t}\tau_{ij} \, {}^{t+\Delta t}e_{ij} \, d^{t+\Delta t} V \\ &= -\int_{t+\Delta t_S} {}^{t+\Delta t}f_i^s \, u_i^s \, d^{t+\Delta t} S \end{aligned} \tag{3}$$

The corresponding governing equation is

$$\begin{aligned} \delta\prod &= \int_{t+\Delta t_V} {}^{t+\Delta t}\tau_{ij} \, \delta \, {}^{t+\Delta t}e_{ij} \, d^{t+\Delta t} V \\ &= -\int_{t+\Delta t_S} {}^{t+\Delta t}f_i^s \, u_i^s \, d^{t+\Delta t} S = 0 \end{aligned} \tag{4}$$

The finite element equilibrium equation for large deformation can also be obtained from eq. (4).

$${}^{t+\Delta t}KU - {}^{t+\Delta t}R = 0 \tag{5}$$

$${}^{t+\Delta t}R = \int_{t+\Delta t_S} H^{sr} \, {}^{t+\Delta t}f^s \, d^{t+\Delta t} S \tag{6}$$

The configuration of the material changes significantly; therefore, as mentioned above, the equilibrium equation of the body must be in the current configuration, not in the initial configuration which is applied in a linear analysis. In addition, the strain-displacement matrix B is no longer constant, and it depends on the element displacements. In order to solve eq. (5), it is necessary to linearize eq. (5) and to divide the nonlinear stiffness matrix ${}^{t+\Delta t}K$ into the

linear and nonlinear terms. In eq. (5) the first term ${}^{t+\Delta t}K\,U$ representing the internal force can be rewritten as ${}^{t+\Delta t}F$, which can be linearized as the following.

$${}^{t+\Delta t}F = {}^{t}F + \frac{\partial {}^{t}F}{\partial {}^{t}U}\,U = {}^{t}F + {}^{t}KU \tag{7}$$

$${}^{t}KU = ({}^{t}K_L + {}^{t}K_{NL})\,U = {}^{t+\Delta t}R - {}^{t}F \tag{8}$$

$${}^{t}K_L = \int_{t+\Delta t_V} {}^{t}B_L^T\, C\, {}^{t}B_L\, d\,{}^{t+\Delta t}V \tag{9}$$

$${}^{t}K_{NL} = \int_{t+\Delta t_V} {}^{t}B_{NL}^T\, {}^{t}\tau\, {}^{t}B_{NL}\, d\,{}^{t+\Delta t}V \tag{10}$$

$${}^{t}F = \int_{t+\Delta t_V} {}^{t}B_L^T\, {}^{t}\bar{\tau}\, d\,{}^{t+\Delta t}V \tag{11}$$

Eq. (8) can not be directly solved for the displacements U since eq. (8) has a fundamental difficulty of the configuration of the body at t+Δt being unknown. Thus, it is necessary to define auxiliary stress and strain measures to express the internal force in eq. (5) in terms of an integral over a known volume allowing incremental decomposition of the stress and strains in an effective manner. By defining the displacement gradient tensor ${}^{t}_{0}X$, the Cauchy-Green deformation tensor ${}^{t}_{0}C$ is obtained. The Cauchy-Green deformation tensor has the following relation of eq. (14) to the Green-Lagrange strain tensor,

$${}^{t}_{0}X = \begin{bmatrix} \frac{\partial {}^{t}x_1}{\partial {}^{0}x_1} & \frac{\partial {}^{t}x_1}{\partial {}^{0}x_2} & \frac{\partial {}^{t}x_1}{\partial {}^{0}x_3} \\ \frac{\partial {}^{t}x_2}{\partial {}^{0}x_1} & \frac{\partial {}^{t}x_2}{\partial {}^{0}x_2} & \frac{\partial {}^{t}x_2}{\partial {}^{0}x_3} \\ \frac{\partial {}^{t}x_3}{\partial {}^{0}x_1} & \frac{\partial {}^{t}x_3}{\partial {}^{0}x_2} & \frac{\partial {}^{t}x_3}{\partial {}^{0}x_3} \end{bmatrix} \tag{12}$$

$${}^{t}_{0}C = {}^{t}_{0}X^T\ {}^{t}_{0}X \tag{13}$$

$${}^{t}_{0}\in = \frac{1}{2}({}^{t}_{0}C - I) \tag{14}$$

where a left superscript indicates the time at which the quantity (body force, surface traction, stress, etc.) occurs, and a left subscript indicates the time with respect to which the quantity is measured.

The 2nd Piola-Kirchhoff stress tensor ${}^{t}_{0}S$, which is the work conjugate with the Green-Lagrange strain tensor ${}^{t}_{0}\in$, which has the following relation to the Cauchy stress tensor ${}^{t}\tau$.

$${}^{t}_{0}S = \frac{{}^{0}\rho}{{}^{t}\rho}\,{}^{0}_{t}X\ {}^{t}\tau\ {}^{0}_{t}X^T \tag{15}$$

Now, employing the total Lagrangian formulation based on eq. (12)~eq. (15), it is possible to refer applied forces, stresses, and strains to a known equilibrium configuration since the configuration of the body at time t+Δt is not known. Subsequently, the integrals in eq. (17)~eq. (19) can be performed.

$${}^{t}_{0}KU = ({}^{t}_{0}K_L + {}^{t}_{0}K_{NL})U = {}^{t+\Delta t}R - {}^{t}_{0}F \tag{16}$$

$${}^{t}_{0}K_L = \int_{0_V} {}^{t}_{0}B_L^T\, {}_{0}C\, {}^{t}_{0}B_L\, d\,{}^{0}V \tag{17}$$

$${}^{t}_{0}K_{NL} = \int_{0_V} {}^{t}_{0}B_{NL}^T\, {}^{t}_{0}S\, {}^{t}_{0}B_{NL}\, d\,{}^{0}V \tag{18}$$

$${}^{t}_{0}F = \int_{0_V} {}^{t}_{0}B_L^T\, {}^{t}_{0}\bar{S}\, d\,{}^{0}V \tag{19}$$

In order to solve eq. (16) at each time step, the Newton-Raphson method is used.

2.2 Hyperelastic model equation

In this study the material to be processed is assumed to be hyperelastic. Even though this assumption does not explicitly take into account time dependent behavior of a polymeric material, it is believed as reasonable because of strong experimental evidence at high strain rates in real thermoforming process[7].

To construct the constitutive equation of the hyperelastic material, Mooney-Rivlin model is adopted as the strain-energy function. This model has been extensively used to solve problems in finite elasticity of rubber at room temperature and thermoplastics at high temperatures.

$$W = \sum_{i=0}^{\infty}\sum_{j=0}^{\infty} A_{ij}(I_1 - 3)^i\,(I_2 - 3)^j \tag{20}$$

Setting i and j as unity, the 2-term Mooney-Rivlin model equation is obtained. It was turned out in the previous study that within moderate stretch ratio, the 2 term Mooney-Rivlin model with reasonable material parameters could predict the deformation behavior properly as well as 5 term Mooney-Rivlin and 6 term Ogden model[8].

$$W = A_{10}(I_1 - 3) + A_{01}(I_2 - 3) \tag{21}$$

At first in this study, 8% sulfur rubber at 20°C is chosen. The two material constants A_{10} and A_{01} are calculated from the regression of Treloar's experimental data of the simple, equi-biaxial extensions, and pure shear experiments[9]. Those material constants are given as follows.

$$A_{10} = 1.85\ \text{kgf/cm}^2,\quad A_{01} = 0.05\ \text{kgf/cm}^2 \tag{22}$$

For the 3-dimensional algorithm the strain energy function

and the stresses are given by

$$W = A_{10}(I_1 - 3) + A_{01}(I_2 - 3) + W_{penalty} + W_{correction} \quad (23)$$

$$S_{ij} = \frac{\partial W}{\partial \in_{ij}} = 2\frac{\partial W}{\partial C_{ij}} \quad (24)$$

where $W_{penalty}$ is added to the strain-energy function to impose the incompressibility condition on the material, and it is shown below with the penalty function $G(I_3)$ with the penalty parameter ε[10].

$$W_{penalty} = \frac{1}{\varepsilon} G^2(I_3) \quad 0 < \varepsilon \ll 1$$

$$G(I_3) = \frac{1}{2} \ln(I_3) \quad (25)$$

In addition, $W_{correction}$ is added to the original strain-energy function to set the value of initial stresses to zero.

$$W_{correction} = -(2A_{10} + 4A_{01})\, G(I_3) \quad (26)$$

For the algorithm with membrane approximation, the stresses in the thickness direction are ignored so as to be expressed much simpler than that of 3-D cases.

$$S_{11} = 2(1 - C_{22}\, C_{33}^2)\left(\frac{\partial W}{\partial I_1} + C_{22}\frac{\partial W}{\partial I_2}\right) \quad (27)$$

$$S_{22} = 2(1 - C_{11}\, C_{33}^2)\left(\frac{\partial W}{\partial I_1} + C_{11}\frac{\partial W}{\partial I_2}\right) \quad (28)$$

$$S_{12} = 2\, C_{21}\, C_{33}^2 \frac{\partial W}{\partial I_1} + 2\left[-C_{12} + C_{33}^2\, C_{21}(C_{11} + C_{22})\right]\frac{\partial W}{\partial I_2} \quad (29)$$

In this case, the incompressibility condition is imposed when we determine the thickness of each element which deforms 2-dimensionally in the absence of the thickness dimension in the 3-dimensional space.

3. Simulation Results and Discussion

3.1 Confirmation of Algorithm

To validate the constructed algorithm, numerical simulations are performed on the simple uniaxial and the equi-biaxial extension systems which have the exact solutions. The nominal stress f or the tensile stress can be obtained from the relation to the strain-energy function below.

$$f_i = \frac{\partial W}{\partial \lambda_i} = \frac{t}{\lambda_i} = \frac{P}{\lambda_i} \quad (30)$$

For the simple extension the material is stretched in the principal direction 1 and equally contracted in the principal directions 2 and 3 according to the incompressible condition, which leads to the principal stretch ratio relation.

$$\lambda_2 = \lambda_3 = \lambda_1^{-\frac{1}{2}} \quad (31)$$

The net nominal stress in the stretching direction 1 is

$$f_1 - f_2 = f = A_{10}\left(2\lambda_1 - 2\frac{1}{\lambda_1^2}\right) + A_{01}\left(2 - 2\frac{1}{\lambda_1^3}\right) \quad (32)$$

For the equi-biaxial extension the material is equally stretched in the principal directions 2 and 3 and contracted in the direction 1, remaining incompressible, and similarly the principal stretch ratio relation is

$$\lambda_1 = \lambda_2^{-2} = \lambda_3^{-2} \quad (33)$$

and the net nominal stress in the stretching direction 2 is the following.

$$f_2 - f_1 = f = A_{10}\left(2\lambda_2 - 2\frac{1}{\lambda_2^5}\right) + A_{01}\left(2\lambda_2^3 - 2\frac{1}{\lambda_2^3}\right) \quad (34)$$

Since the applied pressure P is equal to the nominal force f, it is possible that P in the simulation results is compared with the net nominal stresses calculated exactly in eq. (32) and (34) at the same stretch ratios.

As shown in Fig. 1 and Fig. 2, the simulated results show good agreement with the exact solutions of the simple uniaxial and the equi-biaxial extensions. Therefore, it can be said that the algorithm developed in this study has universal validity.

3.2 Effects of Point Boundary Conditions

In order to apply the algorithm to more complex systems, the free inflation of a rectangular sheet is

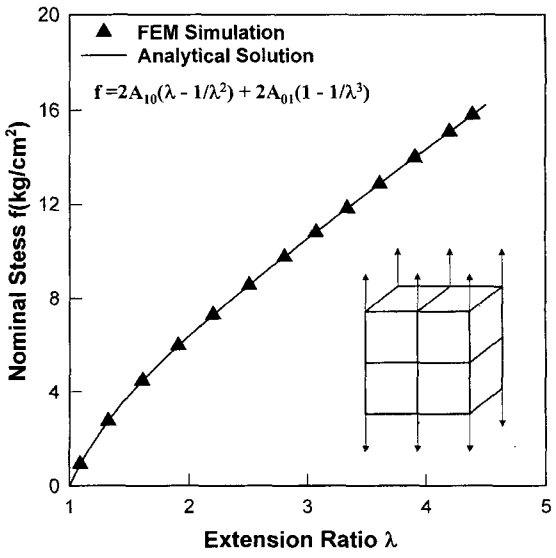

Fig. 1. Comparison of analytical solution with FEM simulation for simple uniaxial extension. A_{10}=1.85, A_{01}=0.05 kgf/cm^2.

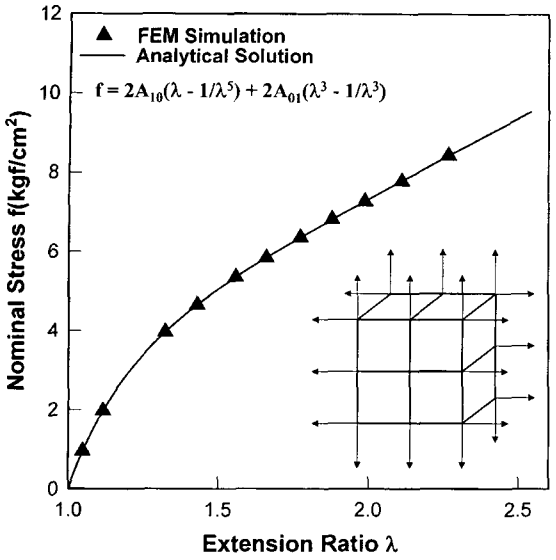

Fig. 2. Comparison of analytical solution with FEM simulation for equi-biaxial extension. A_{10}=1.85, A_{01}=0.05 kgf/cm^2.

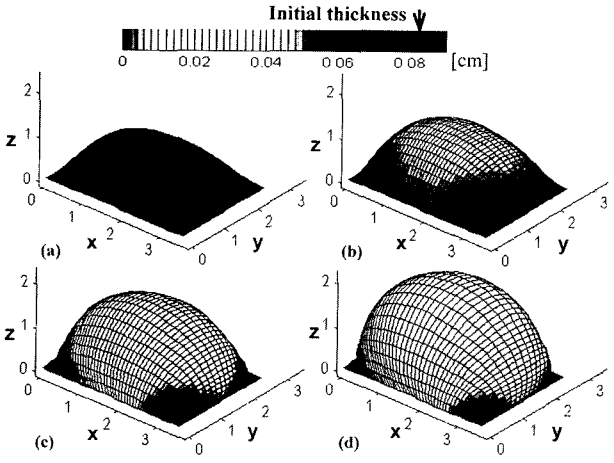

Fig. 3. Consecutive features of free inflation and thickness distribution. Membrane approximation algorithm with initial thickness=0.82 mm. (a) P=0.2396, (b) P=0.3451, (c) P=0.4013, (d) P=0.4174 kgf/cm^2.

simulated first. Fig. 3 illustrates the consecutive features of free inflation with membrane approximated algorithm. The model material is 8% sulfur rubber and the sheet dimension is $2.5\times3.5\times0.082$(width $\times$ length $\times$ thickness) cm. The thickness distribution of the inflated sheet is displayed by colors specified with the color spectrum. As the applied pressure is increased, the inflation proceeds to more extent and the corresponding thickness of each element decreases. As expected, the center of the sheet experiences the largest extension. At a higher pressure of P= 0.4174 kgf/cm^2, wrinkling is observed at the edges of the sheet due to the compressive stresses.

As for the 3-D algorithm it is possible to impose various point boundary conditions such as the simple supported end boundary condition and the clamped end boundary condition. Since the plate has thickness dimension, and more than two layers of nodes exist. The simple supported end boundary condition is to fix the nodes of the single down node layer in the thickness direction, while the nodes of the other node layers remain free. On the other hand, the clamped end boundary condition is to fix the nodes of all the node layers in the thickness direction. In the practical thermoforming process, the point boundary condition is more or less similar to the clamped end boundary condition.

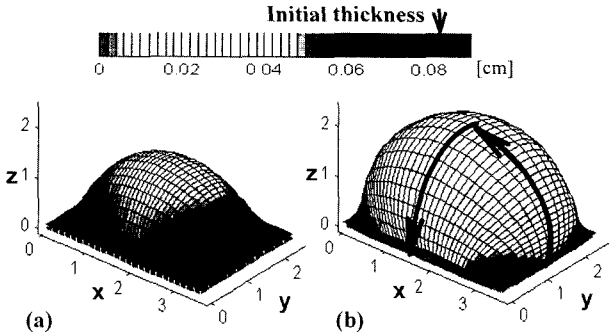

Fig. 4. Comparison of free inflation behaviors with two different boundary conditions. (a) clamped end boundary condition, (b) simple supported end boundary condition. Initial sheet thickness is 0.82 mm, P=0.4174 kgf/cm^2.

Fig. 4 shows the free inflation behaviors of the sheets simulated with the 3-D algorithm when the two different point boundary conditions are imposed. Fig. 4 (a) illustrate when the clamped end boundary condition is imposed, and Fig. 4 (b) the simple supported end boundary condition. It is observed that the case of the 3-D simple supported end boundary condition gives similar inflation shape and thickness distribution as the case of the membrane approximation shown in Fig. 3 (d), while the case of the 3-D clamped end boundary condition differs significantly from it at the same pressure level.

Fig. 5 shows the cross sectional variations of thickness along the arrow direction in Fig. 4 (b) for the membrane approximation case, the 3-D cases of the simple supported end boundary condition and the clamped end boundary condition. Membrane approximation case and the case of the 3-D simple supported end boundary condition are in good agreement and show large deviation from the case of the 3-D clamped end boundary condition. Taking into account that the clamped end boundary condition is closer to the actual boundary condition, it is clear that the membrane approximated algorithm does not offer exact

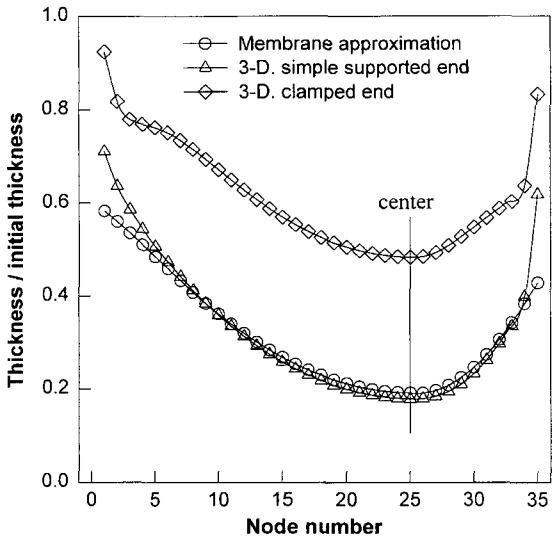

Fig. 5. Thickness variation along the cross sections of free inflated thin gauge sheets with initial thickness=0.82 mm at P=0.4174 kgf/cm^2.

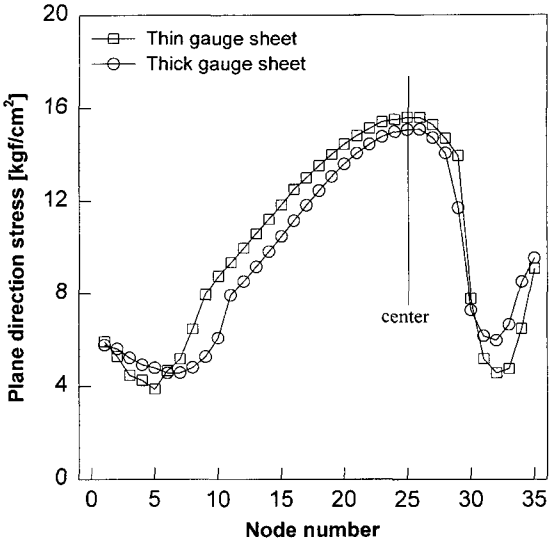

Fig. 7. Comparison of the distribution of plane direction stresses along the arrow direction of sheet for thick(P=0.9490 kgf/cm^2) and thin(P=0.4087 kgf/cm^2) gauge sheets.

prediction of the thickness distribution of sheets.

3.3 Effects of Sheet Thickness

To investigate the effect of sheet thickness, a larger initial thickness of 0.2 cm is considered. The thickness distribution is shown in Fig. 6 with the arrow direction as shown in the Fig. 4. It is observed that even the case of the 3-D simple supported end boundary condition deviates from the membrane approximation case in thickness variation.

From these results, we can conclude that, as the thickness

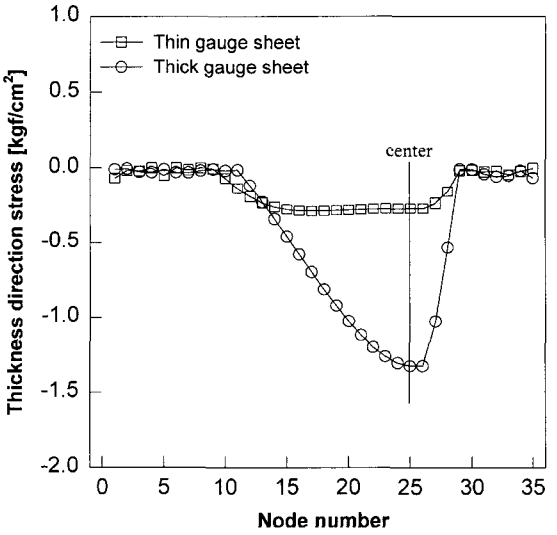

Fig. 8. Comparison of the distribution of thickness direction stresses along the arrow direction of sheet for thick(P=0.9490 kgf/cm^2) and thin(P=0.4087 kgf/cm^2) gauge sheets. The arrow is shown in Fig. 4.

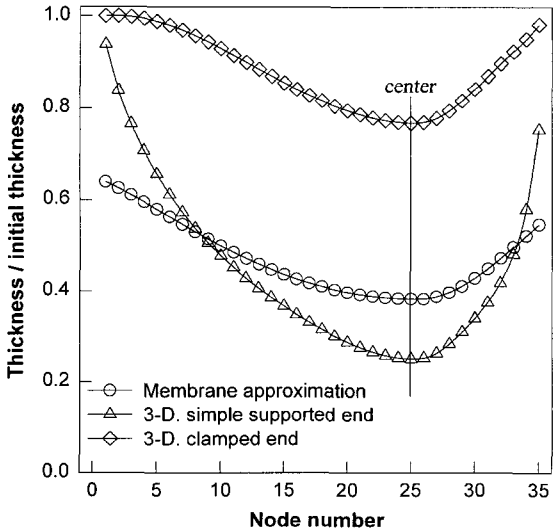

Fig. 6. Thickness variation along the cross sections of freely inflated thick gauge sheets with initial thickness=2 mm at P=0.9490 kgf/cm^2.

increases, the predictability of the membrane approximation quickly deteriorates. The principal stresses are plotted for both the thin and thick gauge sheets and are shown in Fig. 7 and Fig. 8 respectively. Fig. 7 represents the plane direction stresses and Fig. 8 represents the thickness direction stresses with the arrow direction. Plane direction stresses show little deviation between the thin and thick gauge sheets. On the contrary, in case of thickness direction stresses, the thick gauge sheet shows large negative stress value near the center while the thin gauge sheet has nearly zero stress

values. These stress results explain why the inflation behavior of membrane analysis deviates from the 3-dimensional analysis as the thickness increases.

3.4 Effects of Wall Boundary Conditions

A complex concave mold is introduced, and shaping on mold of plastic plates is simulated with the 3-D algorithm. Initial sheet thickness is 0.2 cm. Mold dimensions are 25× 35×17 cm (width×length×depth) and 1 0 cm depth of block is located at center. In the case of shaping on mold, wall boundary conditions should be considered. We use the slip and the no-slip boundary condition to give constraints to the plates contacted with molds.

Fig. 9 shows the consecutive features of the no-slip mold shaping with the 3-D algorithm. The thickness distribution is displayed by the color spectrum. In Fig. 9 (b) the center region of the plate begins to be contacted with the mold at P=0.4025 kgf/cm^2, and it cannot inflate further, so that the thickness remains almost the same while the neighboring elements inflate and their thickness get thinner. As the pressure increases, each element, especially the elements at the edge which contact with the inside corners of the mold, continues stretching so as to have the thickness ratio to the initial thickness almost one eighth.

Fig. 10 shows the thickness variation along the arrow direction of the plates. For the membrane approximation cases and the 3-D cases of the simple supported end boundary condition with the slip and the no-slip boundary condition is imposed. Slip boundary conditions have

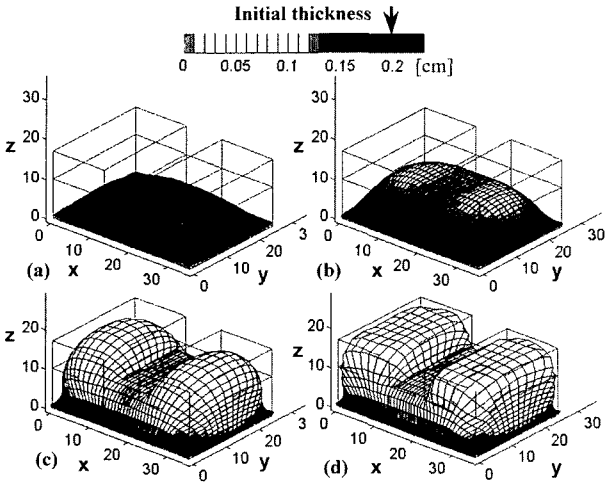

Fig. 9. Consecutive features of no-slip mold shaping and thickness distribution. 3-dimensional algorithm with simple supported end boundary condition. Initial thickness=2 mm. (a) P=0. 2038, (b) P=0.4025, (c) P=0.8045, (d) P=1.8041 kgf/cm^2.

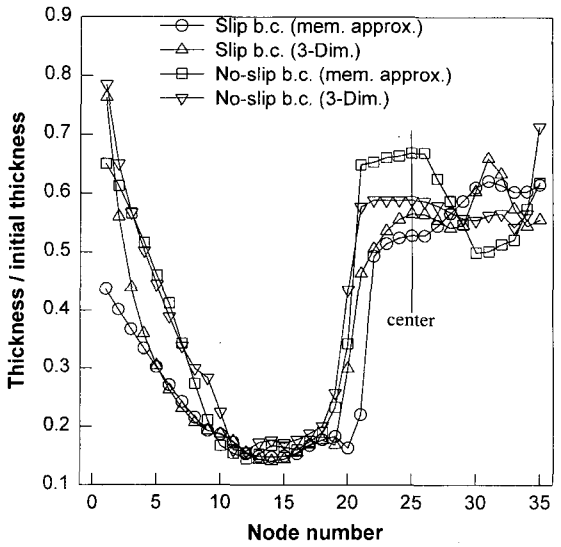

Fig. 10. Thickness variation along the arrow direction of sheets shaped on mold with initial thickness=2 mm at P=1.8041 kgf/cm^2. The arrow is shown in Fig. 4.

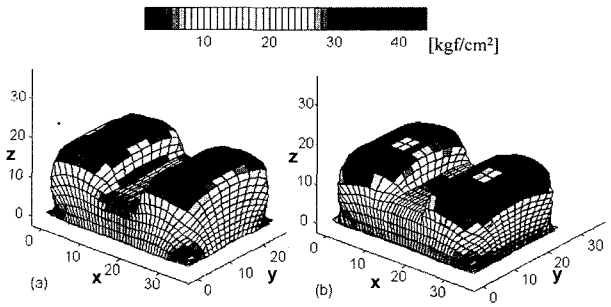

Fig. 11. Features of slip and no-slip mold shaping and stress distribution. Initial thickness=2 mm. 3-dimensional algorithm with simple supported end boundary condition. (a) Slip mold boundary condition, (b) No-slip mold boundary condition at P=1.8041 kgf/cm^2.

relatively thinner at center and become thicker at edge. In contrast, no slip boundary conditions have thicker at center and become thinner at edge. The thickness distribution becomes even in case of slip boundary conditions. Even for the same boundary condition, 3-D and membrane analysis has quite a large deviation.

Fig. 11 (a) and (b) illustrate respectively the two features of the slip and the no-slip mold shaping and the stress distribution at P=1.8041 kgf/cm^2 with the 3-D algorithm. The stresses displayed are two principal stresses in the direction of the plane. The slip case also has relatively uniform stress distribution, while the no-slip case has high stress at the edge.

In the practical thermoforming process, there exists some friction between the metal wall of the mold and plastics being formed. Thus, the no-slip case is more or

less closer to the actual situation even though both the slip and the no-slip cases are extreme. However, in order to perform more accurate simulation it is suggested that the friction coefficient between the mold and the plate should be used by the algorithm.

3.5 Effect of sheet temperature

Hot tensile test data of ABS material is used to investigate the effect of processing temperature. Test temperature ranges from 137.8°C to 171.1°C, which is common processing temperature range of ABS[11]. Also, crosshead rate is 1.05 in/sec which is quite large and is representative of thermoforming rates. Fig. 12 represents the stretch ratio vs. true stress data. As the temperature increases, stress dramatically decreases. The solid line in this figure is generated from a nonlinear least squares curve fit of the experimental data using a 2-term Mooney-Rivlin model. From this figure it can be seen that 2-term Mooney-Rivlin model can represent the data for simple uniaxial extension reasonably well over a large strain range.

The material parameters for each temperature are listed in Table 1. As the temperature increases, A_{10} decreases and A_{01} increases. Six times of A_{10} and A_{01}, the elastic modulus for

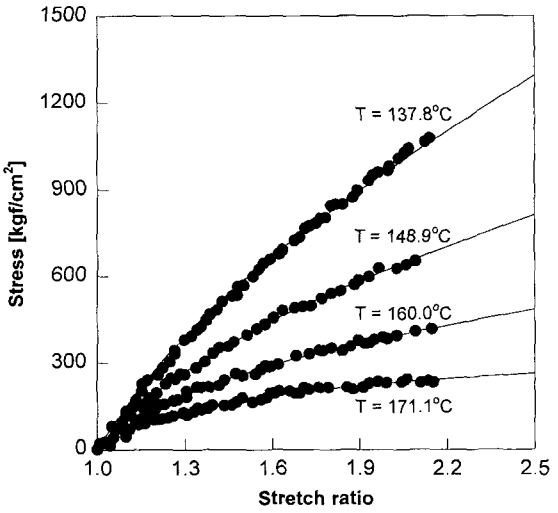

Fig. 12. Stress vs. stretch data for ABS resin. Curve fits using the 2-term Mooney-Rivlin model and displacement rate is 1.05 in/sec.

Table 1. 2-term Mooney-Rivlin constants of ABS for various temperatures

Temperature[°C]	A_{10}[kgf/cm²]	A_{01}[kgf/cm²]
137.8	2.89	0
148.9	1.63	0.46
160.0	0.76	0.81
171.1	0.20	0.97

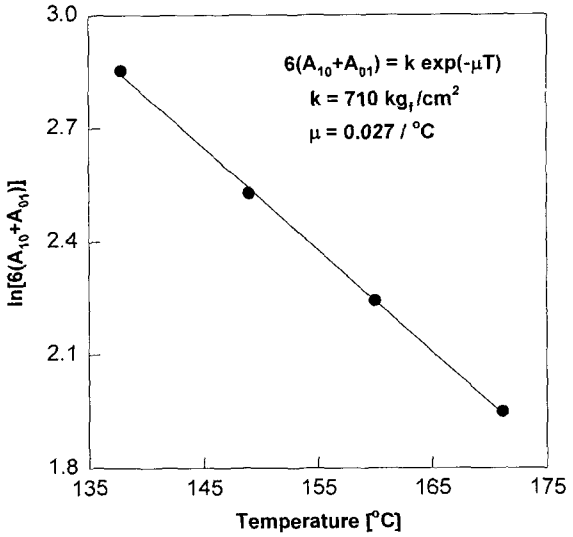

Fig. 13. Temperature dependence of 2-term Mooney-Rivlin parameter of ABS resin for uniaxial-stretching results.

infinitesimal deformations, decreases as a function of increasing time. Using a least squares curve fit, a temperature dependence of $6(A_{10}+A_{01})$ can be empirically correlated with temperature using an Arrhenius type exponential expression of the form. This is plotted in Fig. 13, which lies in a single line exactly.

$$6(A_{10}+A_{01}) = k\exp(-\mu T) \tag{35}$$

The calculated values are k=710 kgf/cm², μ=0.027/°C.

At each temperature, inflation behaviors of rectangular sheet are numerically simulated. The thickness distributions

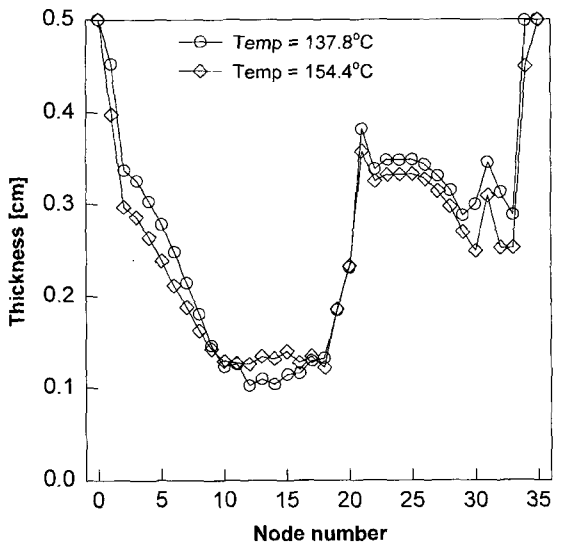

Fig. 14. Thickness distribution of ABS sheets along the arrow direction for low and high processing temperatures. Initial thickness=5 mm.

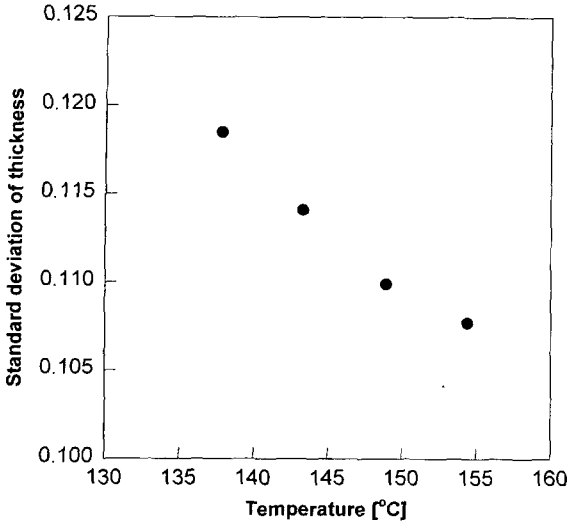

Fig. 15. Standard deviation of thickness for various processing temperatures.

with the arrow direction are shown in Fig. 14 for T=137.8 °C and T=154.4°C. At the high sheet temperature, the thickness of thinnest part becomes thick and the thickest part thin. The thickness of the finally deformed sheet is more evenly distributed at higher sheet temperature. This is because, as the sheet temperature increases, the fluidity of sheet increases. The evenness of thickness distribution can be confirmed by checking the standard deviation of thickness. The effect of sheet temperature on the standard deviation of thickness is plotted in Fig. 15. It can be clearly understood that as the temperature increases, more even thickness distribution is achieved.

4. Conclusion

In this study the 3-D simulation algorithm and the membrane approximation algorithm of the thermoforming process are developed. The algorithm has been validated that the simulation results show good agreement with the exact solutions for the simple and the equi-biaxial extensions. The effects of the point boundary conditions, the initial thickness of sheets and plates, the wall boundary conditions, and the sheet temperature on the inflation behaviors of plastics are investigated together with the stress analysis. The main results are summarized as following.

1. The point boundary conditions have considerable effects on the inflation behaviors of plastic sheets and plates. The membrane approximation algorithm gives good agreement with the 3-D algorithm with the simple supported end boundary condition, while it does not with the 3-D algorithm with the clamped end boundary condition.

2. The membrane approximation algorithm shows large deviation from the 3-D algorithm in the thickness distribution of relatively thick plates. This can be explained by the stress analysis of thick and thin sheet.

3. The wall boundary conditions affect the final properties of thermoformed products such as thickness and residual stresses.

4. The thickness variation can be evenly distributed as increasing the sheet temperature, which is due to the sheet fluidity.

5. Nomenclature

Roman Letters

$^{t}B_{L}$, $^{t}{}_{0}B_{L}$ = linear strain-displacement transformation matrices

$^{t}B_{NL}$, $^{t}{}_{0}B_{NL}$ = nonlinear strain-displacement transformation matrices

C = stress-strain material property matrix

$_{0}C$ = incremental stress-strain material property matrix

e_{ij} = Cartesian components of the strain tensor

$^{t+\Delta t}\delta e_{ij} = \frac{1}{2}\left(\frac{\partial \delta u_i}{\partial {}^{t+\Delta t}x_j} + \frac{\partial \delta u_i}{\partial {}^{t+\Delta t}x_j}\right)$ = strain tensor

f_1, f_2, f_3 = nominal stress

f_i^s = components of externally applied surface tractions per unit surface area at time t+Δt

^{t}F, $^{t}{}_{0}F$ = vectors of nodal point forces equivalent to the element stresses at time t

H^s = surface-displacement interpolation matrix

I_1, I_2, I_3 = first, second, and third invariants

$^{t}K_{L}$, $^{t}{}_{0}K_{L}$ = linear strain incremental stiffness matrices

$^{t}K_{NL}$, $^{t}{}_{0}K_{NL}$ = nonlinear strain incremental stiffness matrices

P = pressure applied to the surface of sheets

$^{t+\Delta t}R$ = vector of externally applied nodal point loads at time t+Δt

S = initial area

$^{t+\Delta t}S$ = area at time t+Δt

$^{t}{}_{0}S_{ij}$ = matrix components of 2nd Piola-Kirchhoff stress

t_i = tensile stress (true stress)

U = vector of increments in the nodal point displacements

u_i = components of displacements

δu_i = components of virtual displacement vector

impos- ed on configuration at time t+Δt, a function of ${}^{t+\Delta t}x_j$, j = 1, 2, 3

δu_i^s = δu_i evaluated on the surface ${}^{t+\Delta t}S$ (the δu_i components are zero at and corresponding to the prescribed displacements on the surface ${}^{t+\Delta t}S_u$)

V = initial volume

${}^{t+\Delta t}V$ = volume at time t+Δt

W = stain-energy function

${}^{t+\Delta t}X_j$ = Cartesian coordinates of material point at time t+Δt

Greek Letters

$\lambda_1, \lambda_2, \lambda_3$ = principal stretch ratio

$\prod$ = total potential energy

${}^t\tau$, ${}^t\vec{\tau}$ = matrix and vector of Cauchy stresses

${}^{t+\Delta t}\tau_{ij}$ = Cartesian components of the Cauchy stress tensor

References

1. J. T. Oden and T. Sato, *Int. J. Solids Structures,* **3**, 471-488 (1967).
2. W. W. Feng and P. Huang, *J. Appl. Mech.*, 767 (1974).
3. H. G. deLorenzi and H. F. Nied, *Comp. Structures,* **26**, 197-206 (1987).
4. W. N. Song, F. A. Mirza, J. Vlachopoulos, *J. Rheol,* **35**, 93 (1991).
5. N. G. Zamini, D. F. Watt, M. Esteghamatian, *Int. J. Numer. Methods Eng.,* **28**, 2681 (1989).
6. K. J. Bathe, "Finite Element Procedures", Prentice-Hall, Inc., NJ (1996).
7. H.G. deLorenzi and C.A. Taylor, *Intern. Polymer Processing,* **VIII**, 365 (1993).
8. G.J. Nam and J.W. Lee, The Korean *J. of Rheol., vol.***8**, no.3+4, p215 (1996).
9. L. R. G. Treloar, *Trans. Faraday Soc.,* **40**, 59-70 (1944).
10. M. S. Gadala, *J. Comp. Struct.,* **42**, 1-10 (1992).
11. J. Goldsmith, "High temperature/high speed tensile testing of amorphous and crystalline polymers", Master Thesis, University of Louisville (1987).
12. A. E. Green and J. E. Adkins, "Large Elastic Deformations and Nonlinear Continuum Mechanics," Oxford University Press, Oxford, 1970.
13. J. T. Oden, "Finite Elements of Nonlinear Continua", McGraw-Hill, Inc., NY, 1972.
14. R. I. Tanner, "Engineering Rheology", Clarendon Press, Oxford (1985).
15. T. J. Chung, "Continuum Mechanics," Prentice-Hall, 1988.
16. H.G. deLorenzi and H.F. Nied, "Modeling of Polymer Processing", ed., by A.I. Isayev Hanser Verlag, Munchen, 1991, p117.
17. W. N. Song, F. A. Mirza, J. Vlachopoulos, *Intern. Polymer Processing* **VII**, 248-256 (1992).
18. D. Laroche and F. Erchiqui, *SPE ANTEC Tech. papers,* **56**, 676 (1998).
19. B. Debbaut, O. Homerin, A. Goublomme and N. Jivraj, *SPE ANTEC Tech. papers,* **56**, 1824 (1998).
20. G.J. Nam, J.S. Lee, H.M. Park and J.W. Lee, Proceeding of '95 KIChE spring meeting, p733-736 (1995).
21. G.J. Nam, D.S. Son and J.W. Lee, Proceedings of KSOR fall meeting, p40-43 (1996).
22. G.J. Nam, D.S. Son and J.W. Lee, PPS Europe/Africa regional meeting, August 19-21, Gothenburg, Sweden (1997).
23. G.J. Nam, H.W. Rhee and J.W. Lee, *SPE ANTEC Tech. papers,* **56**, 681 (1998).
24. G.J. Nam and J.W. Lee, J. of Reinforced Plastics and Composites, in press (1999).